J Therm Spray Tech
DOI 10.1007/s11666-017-0619-5

PEER REVIEWED

# Effects of Traverse Scanning Speed of Spray Nozzle on the Microstructure and Mechanical Properties of Cold-Sprayed Ti6Al4V Coatings

**Adrian Wei-Yee Tan[1,2] · Wen Sun[1,2] · Yun Peng Phang[2] · Minghui Dai[2] · Iulian Marinescu[1,3] · Zhili Dong[4] · Erjia Liu[1,2]**

Submitted: 17 March 2017 / in revised form: 13 August 2017


**Abstract** Cold spray has the potential to restore damaged aerospace components made from titanium alloy, Ti6Al4V at low temperature (200-400 °C). Traverse scanning speed during deposition is one of the key factors that affect the quality of the Ti6Al4V coatings as it influences the thermal build-up and coating thickness per pass. As there are fewer reported studies on this, this work investigated the effects of different traverse scanning speeds (100, 300 and 500 mm/s) of cold spray nozzle on the microstructure and mechanical properties of cold-sprayed Ti6Al4V coatings. The cross-sectional analysis showed coating porosities reduces with slower traverse speed, from 3.2 to 0.5%. In addition, the microhardness of the coatings increased from about 361-385 HV due to strain hardening. However, the adhesion strength of the coatings to the substrates significantly decreased with reduced traverse speed from about 60 MPa (glue failure) at 500 mm/s to 2.5 MPa (interface failure) at 100 mm/s. Therefore, this study revealed that the control of heat build-up and thickness per pass during the cold spray deposition of the Ti6Al4V coatings is crucial to attain the desirable properties of the coatings.

**Keywords** cold spray · traverse scan speed · Ti6Al4V coating · Ti6Al4V substrate · heat accumulation · microstructure · mechanical properties

✉ Erjia Liu
mejliu@ntu.edu.sg

Adrian Wei-Yee Tan
adriantan@ntu.edu.sg

[1] Rolls-Royce@NTU Corporate Lab, Nanyang Technological University, 50 Nanyang Avenue, Singapore 639798, Singapore

[2] School of Mechanical and Aerospace Engineering, Nanyang Technological University, 50 Nanyang Avenue, Singapore 639798, Singapore

[3] Advanced Technology Centre, Rolls-Royce Singapore Pte Ltd, 1 Seletar Aerospace Crescent, Singapore 797575, Singapore

[4] School of Materials Science and Engineering, Nanyang Technological University, 50 Nanyang Avenue, Singapore 639798, Singapore

## Introduction

Titanium alloys are widely used in aircraft because they have lightweight, high specific strength (up to 400 °C) and excellent corrosion resistance. In particular, Ti6Al4V or Ti64 in short is used in various sections of an aircraft such as fuselage, nacelles, landing gears, fan disks and blades (Ref 1, 2). However, these components do suffer from damage during service (e.g., erosion and abrasion) and require restoration. Thermal spray and welding have been utilized for aviation repair industry because of their adaptability and an extensive variety of applicable materials (Ref 3). However, as these processes involve melting and resolidification of materials, they lead to undesirable effects such as high oxidation level, high thermal residual stress, and limited thickness build-up.

Cold spraying is highly suitable for temperature sensitive materials such as Ti64. It is a process where microparticles are accelerated to supersonic speeds and then deposited on a target substrate surface to build a dense coating (Ref 4-10). These particles are bonded at solid state (no melting), and the bonding mechanism is adiabatic shear instability and mechanical interlocking. The benefit of cold spraying is low thermal input and no microstructural changes to the particles and base material. These properties make cold spraying a competitive technology for repair as

Published online: 23 August 2017

it is economically advantageous (Ref 11), has good performance and has been incorporated into a repair facility or as part of production (Ref 12).

The overall quality of cold-sprayed Ti64 coatings can be significantly influenced by cold spray process parameters such as type of working gas, working gas pressure and temperature, on which many investigations have been reported (Ref 13-24). One of the current gaps for Ti64 deposition is the effect of traverse scan speed of cold spray nozzle, which is critical as it affects the heat accumulation and deposition thickness per pass in the coatings. So far, studies on traverse speed were only conducted for aluminum 6061 (Al 6061) (Ref 25) and commercially pure titanium (CP Ti) (Ref 26). The studies showed that, to reach a similar coating thickness, a slower scan speed (or a thicker layer per pass) resulted in a higher substrate temperature as compared to a faster scan speed (or a thinner coating per pass), which promoted more severe deformations of the sprayed particles thus leading to a denser coating. At slower traverse speed of deposition, the Al 6061 coating also showed an increment of adhesion strength and hardness, which could be due to the reduced tensile peaks between coating layers and a higher shot peening effect, respectively. As for the study on CP Ti, the deposition at slower traverse speed demonstrated a lower coating hardness, which was suggested to be the predominant annealing effect of static recovery, although dynamic recovery and dynamic recrystallization might have occurred during the deposition process. The increased presence of oxides and nitrides was also detected in the coating formed at slower traverse speed (higher substrate temperature). However, the CP Ti coating (deposited at lower traverse speed) remained in good quality (high plastic deformation and low porosity level), which can be explained by the breakdown of oxides and nitrides layers upon impact by the sprayed particles.

Therefore, with reference to the literature, it will be interesting to understand the effects of traverse scan speed of spray nozzle on the characteristics of Ti64 coatings. This paper systemically investigated the microstructure and mechanical properties of cold-sprayed Ti64 coatings in terms of traverse scan speed of spray nozzle.

## Experimental Details

### Materials

Ti64 (Grade 5) disks (Titan Engineering, Singapore) with 25 mm diameter and 5 mm thickness were used as substrates. The substrates were ground and degreased sequentially before cold spray deposition. The powder used as the feedstock was plasma-atomized spherical Ti64 ELI (Grade 23) (Fig. 1a, b) with the average size ranging from 15 to 45 μm as shown in Fig. 1(c). The particle size distributions measured by laser diffraction (ASTM B822-10) for D10, D50 and D90 were 18, 31.6 and 43.5 μm, respectively (Ref 27). The EDS result in Fig. 1(d) showed no impurities present in the particles.

### Cold Spray Deposition

All Ti64 coatings were deposited using an Impact Spray system 5/11 with a SiC spray nozzle (Impact Innovations, Germany), with the setup shown in Fig. 2(a). The nozzle had a 6 mm diameter round outlet, an expansion ratio of 5.6, and a divergent section length of 160 mm. The deposition details are shown in Table 1.

During the deposition, the sample stage was moved in a zig-zag pattern with a constant velocity, i.e., 100, 300 and 500 mm/s, followed by a 1 mm vertical step after each traverse movement (Fig. 2b) to form a coated layer, while the cold spray gun remained in a stationary position. With all the parameters maintained, due to surface interaction time, each traverse speed deposited different thickness per layer and the final coating thicknesses were within 2.3-3 mm. For easy reference, the coatings deposited at 100, 300 and 500 mm/s were referred to as $T_{100}$, $T_{300}$ and $T_{500}$, respectively.

### Temperature Measurement

The temperatures of gas impingement and particle deposition were measured based on the parameters illustrated in Table 1. Figure 3 shows that a K-type thermocouple was sandwiched in between two Ti64 substrates (50 mm × 50 mm × 4 mm). The data were logged using Omega TC-08 (USA) at a frequency of one measurement per second. The data recording was started at 100 °C to avoid the influence of different approaches of the sample and gun (Ref 25). A visual inspection on the substrate surface color was also carried out after each temperature measurement.

### Characterization

The surface roughness profiles, $R_a$, of the coatings were measured using 3D measurement macroscope (Keyence VR-3100, Keyence Co., Japan), which had a precision of ± 0.5 μm. Four measurements were taken from each surface, with an evaluation length of 6.4 mm and a cut-off length of 0.8 mm.

For cross-sectional analysis, each cold-sprayed sample was cut into halves with coating dimensions of 25 mm (length) × 7.3-7.8 mm (thickness). The cut samples were then hot mounted with Polyfast, ground with MD-Mezzo

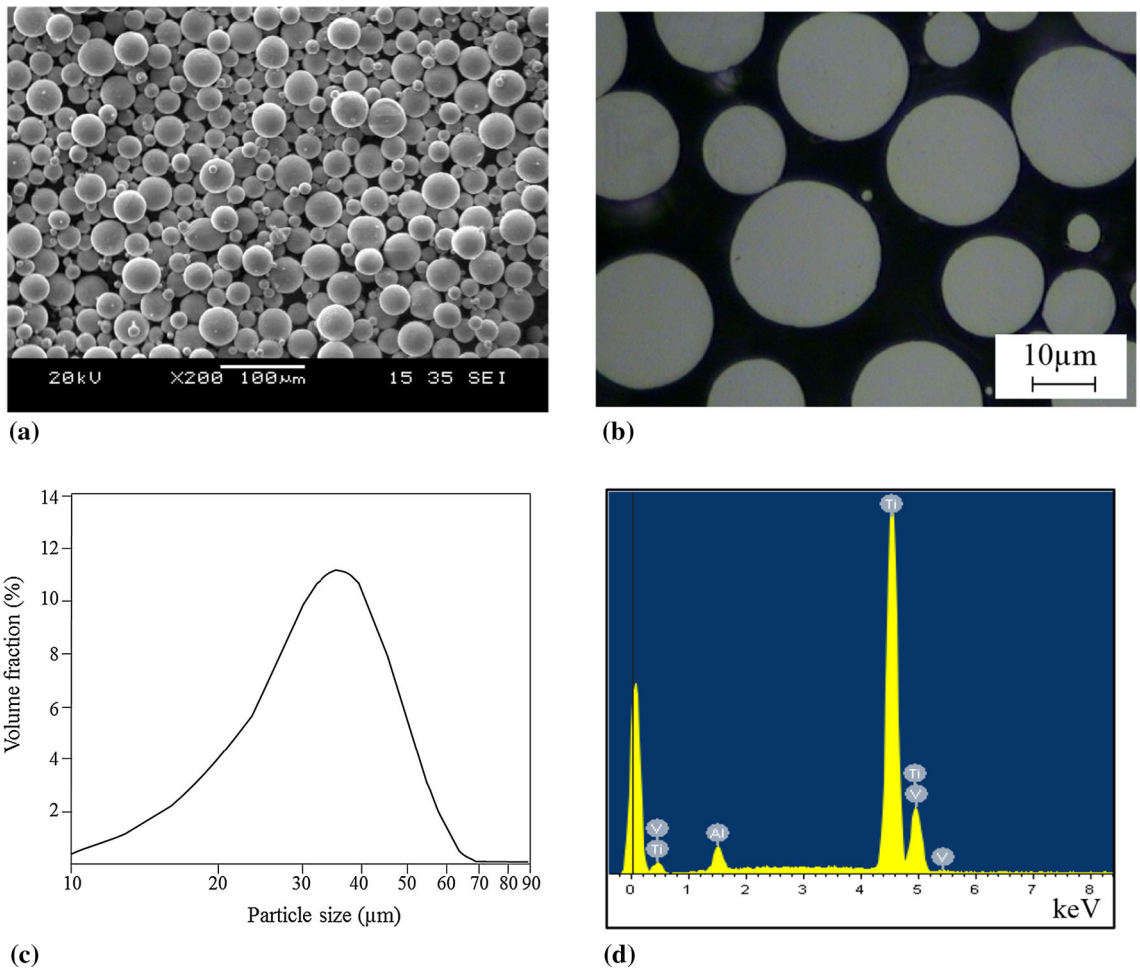


**Fig. 1** (a) SEM micrograph of pristine Ti64 powder, (b) optical micrograph of polished cross section of Ti64 particles, (c) particle size distribution and (d) EDS spectrum of Ti64 powder

**Fig. 2** (a) Cold spray setup and (b) scanning steps (the drawing is not to scale)

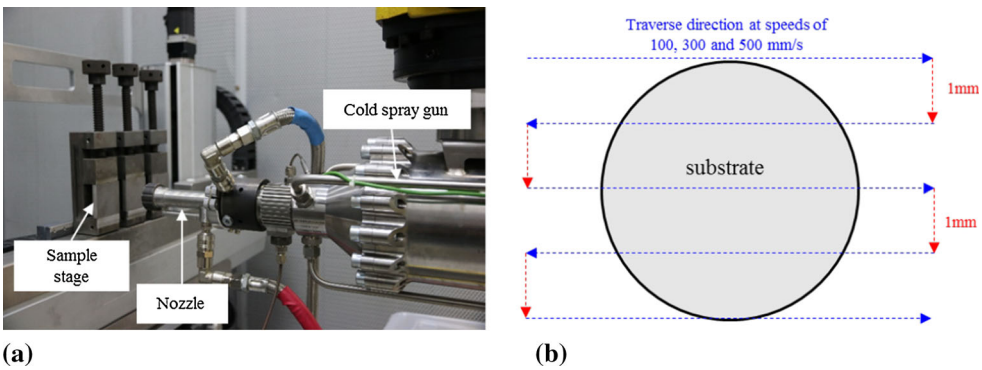


(comparable with #220 grit SiC foil), followed by chemical–mechanical polishing (CMP) with a DiaPro solution containing 9 µm diamond particles and then an OP-S suspension solution containing 0.04 µm colloidal silica particles (Struers, Denmark). The polished samples were etched for the microstructural evaluation using Kroll's reagent by immersion method for 10-15 s.

Microstructures and porosities of the samples were observed under optical microscopy (OM, Axioskop 2 MAT, Carl Zeiss, Germany) and/or scanning electron microscopy (SEM, JSM-5600LV JEOL, USA) operated at 15-20 kV. For porosity measurement, a series of 16 continuous cross section images (optical micrographs ×200 magnification) were taken from the coating top, middle and

near-interface regions. These images were stitched (per location) and processed using open source software ImageJ (NIH, USA) (Ref 24).

Elemental compositions of the samples were analyzed using energy-dispersive spectroscopy (EDS, Oxford Instrument, UK). Phase analysis of the cold-sprayed samples was carried out using Philips PW1830 x-ray diffractometry (XRD, Netherlands) with Cu $K_\alpha$ radiation at 30 kV and 20 mA, from 20 to 90 degrees of $2\theta$.

Microhardness of each sample was evaluated using a Vickers microindenter, (FM-300e, Future-Tech, Japan), with a 300 g load. A total of 10 indents were randomly made across the cross section of the sample, and an average hardness value was calculated. On the other hand, the hardness of the Ti64 powder was measured using a nanoindenter (G200, Agilent, USA) with a load of 30 mN and a penetration depth of 1 µm. Around 15 particles with diameters around 20-40 µm were indented to ensure that the penetration was within the particles rather than the epoxy resin.

Adhesion strength test was conducted on each coated sample thickness according to the standard ASTM C633 (Ref 28). First, the coated Ti64 sample was slightly ground flat to smoothen the surface while maintaining the original coating thickness. Next, the surface of the sample and stainless steel fixture were sand blasted with P80 alumina particles, cleaned with ethanol and assembled with an adhesive glue (Araldite AV170, Huntsman Advanced Materials, USA). The assembled set was then placed at a tilt angle of 35° in an oven in which the set was cured at 150 °C under a weight of 380 g for 60 min and left to cool to room temperature. The set was tested using Instron 5569 (UK), with a load cell of 50 kN in tensile mode at an extension rate of 0.8 mm/min till the set failed.

**Table 1** Cold spray deposition details

| Parameter | Unit | Sample ID | | |
|---|---|---|---|---|
| | | $T_{100}$ | $T_{300}$ | $T_{500}$ |
| Sample-stage traverse speed | mm/s | 100 | 300 | 500 |
| Working gas | | | Nitrogen | |
| Gas pressure | MPa | | 4.5 | |
| Gas temperature | °C | | 1000 | |
| Spray angle | ° | | 90 | |
| Stand-off distance | mm | | 30 | |
| Raster step | mm | | 1 | |
| No. of passes | | 4 | 10 | 18 |
| Coating thickness per pass | mm | 0.75 | 0.28 | 0.13 |
| Coating thickness | mm | 3 | 2.8 | 2.3 |

## Results and Discussion

### Temperature Analysis

Figure 4 shows the independent temperature measurements of gas impingement (Fig. 4a) and coating deposition onto the substrates (Fig. 4b) at different traverse speeds. Figure 4(a) and (b) indicates that the substrate temperature reduces with increasing traverse speed. At traverse speeds of 100, 300 and 500 mm/s, the maximum measured temperatures for gas impingement were 358.7, 348.2 and 332.5 °C, respectively, while those for coating deposition were 366, 354.4 and 315 °C, respectively. This phenomenon can be explained using the heat formula (Eq 1) and traverse speed (Eq 2):

$$q = \frac{Q}{t_{\text{heat}}} = \frac{mc\Delta T}{t_{\text{heat}}} \quad \text{(Eq 1)}$$

where $q$ is the heat flux, $t_{\text{heat}}$ is the heating time, $m$ is the mass of flow, $c$ is the specific heat, and $\Delta T (= T_{\text{sub}} - T_{\text{surr}})$ is the change in temperature with $T_{\text{sub}}$ being the substrate and $T_{\text{surr}}$ the surrounding temperatures.

$$v = \frac{d}{t} = \frac{d}{t_{\text{heat}}} \quad \text{(Eq 2)}$$

where $v$ is the stage traverse speed, $d$ is the distance travelled and $t$ is the time that can be equal to heating time, with respect to the gun location. The relationship of Eq 1 and 2 shows that $v$ is inversely proportional to $m$ and $\Delta T$, which means that a lower traverse speed allows a longer heating time which increases the substrate temperature relative to the surrounding temperature and mass of flow (per location), and vice versa.

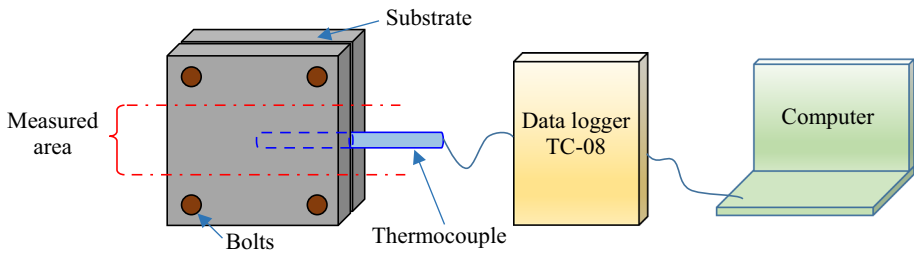


**Fig. 3** Substrate temperature measurement setup

In each temperature profile in Fig. 4(b), there were multiple fluctuations in temperature which formed a wave-like pattern of peaks and valleys. As there was only a thermocouple positioned in the fixture, the highest peak was when the gas/particle stream directly passed through the thermocouple and the valleys were the when the gas/particle stream was at the furthest location from the thermocouple. The temperature frequency (based on a period of peak to peak at steady state) of 100 mm/s traverse speed was the lowest (0.083 Hz), followed by 300 (0.2 Hz) and 500 mm/s (0.33 Hz). These frequencies showed that the thermal distribution was more uniform for higher traverse speeds which may be better for stress distribution. This is crucial when depositing coatings onto large surface areas. As the material properties are temperature dependent, the deposition strategy has to ensure similar temperature profile through the passes for uniform stresses.

One of the most important observations is that the differences of the maximum temperatures from gas impingement and particle deposition are quite small, i.e., 7.3, 6.2 and 17.5 °C for 100, 300 and 500 mm/s, respectively. The small temperature differences reinforce the adiabatic shear instability theory where the heat from the impact of particles is not conducted away and used for high-strain-rate deformation with shear localization (Ref 29, 30).

Heat tinting on the substrate surface can be observed after the temperature measurement of the impinged gas as shown in Fig. 5. The substrate surface impinged by the $N_2$ gas at a traverse speed of 100 mm/s has a heat tint of purple color (Fig. 5a) as compared to a yellow color corresponding to 300 and 500 mm/s (Fig. 5b). The surface temperature for titanium to develop purple color is estimated to be around 412°C, while yellow color is around 385 °C (Ref 31). The color changes are an indication of thickness variations of the oxide film from about 50 to 200 nm, due to light interference phenomenon at the metal–oxide–air interfaces (Ref 32, 33). The slow traverse speed and rapid thermal build-up allow sufficient time for chemical reaction to occur to form a thicker oxide layer. If the substrate undergoes an uncontrolled preheating cycle before deposition, the sub-surface layer of the substrate might have a thick oxide film, which will negatively affect the particle bonding.

## As-Sprayed Surface and Cross-Sectional Analysis

The coating surface roughness, $R_a$, decreases with increasing traverse speed where deposition at traverse speed of 100, 300 and 500 mm/s was 8.89, 8.76 and 7.23 µm, respectively. This could be attributed to the coating thickness per pass, where more number of layers result in lower surface roughness due to more even distribution of particle deformation. However, the maximum difference of surface roughness among the samples is only 1.7 µm (20%), which is not large. Based on particle

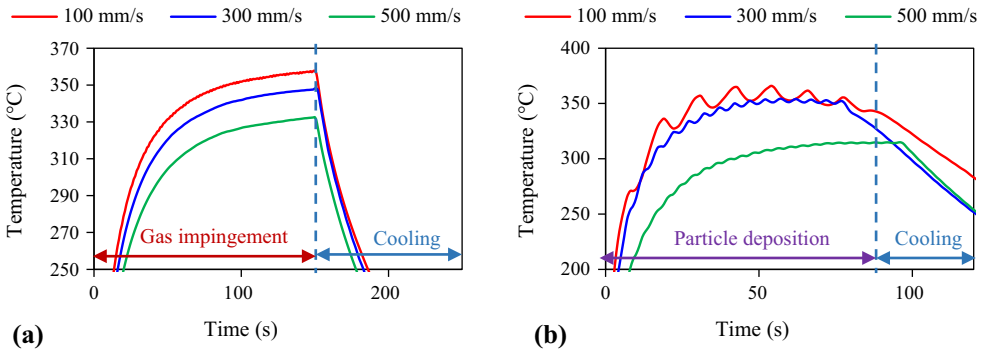


**Fig. 4** Temperature profiles as a function of time of (a) gas impingement and (b) during particle deposition

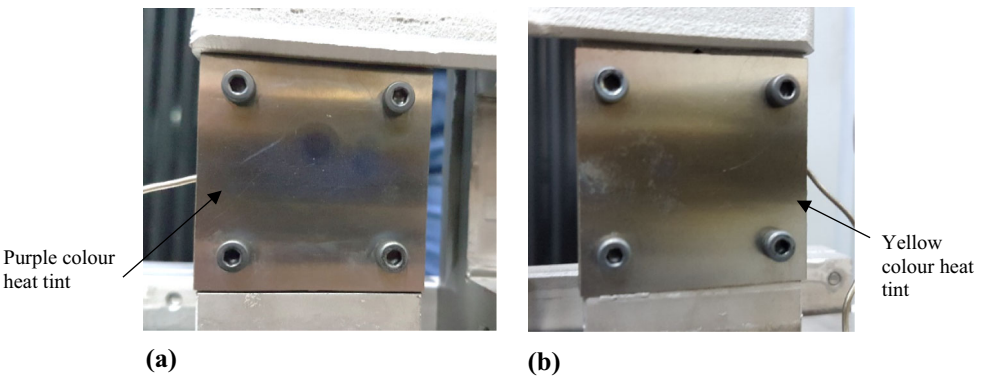


**Fig. 5** Photographs showing heat tint on Ti64 substrates during gas temperature measurement at a traverse speed of (a) 100 and (b) 300 mm/s. The heat tint with respect to 500 mm/s is not shown due to its similarity with that with respect to 300 mm/s

morphologies in Fig. 6(d-f) and the polished cross section of the coatings in Fig. 6(g-i), particles were observed to be heavily plastically deformed with material jetting and have a similar aspect ratio (width/height of particle), as a result of deposition at similar particle velocities.

The cross section of the samples is shown in Fig. 7 (optical micrographs) and Fig. 8 (SEM micrographs). The interface of $T_{100}$ sample had severe delamination, with only 10% bonded (Fig. 7a) which was caused by shattered substrate sub-surface layer (24 μm thick), observed under SEM in Fig. 8(c). Interestingly, the delamination was not purely de-bonding of the coating from the substrate, but from a shattered substrate sub-surface from its bulk material. EDS of the shattered sub-surface layer showed that it is not an oxide layer, where the composition is still 91% titanium, 5.4% aluminum and 3.6% vanadium. The delamination might also serve as a crack propagation to the other parts the interface. Sample $T_{100}$ also has a non-uniform behavior throughout the coating section with the presence of inter-particle cracking (Fig. 8a) as compared to other sections (Fig. 8b). The cause could be due to unbalanced residual stress resulting from non-uniform thermal expansion and shrinkage, based on thermal fluctuation in Fig. 4(b), as well as the effect of thickness per layer during deposition (Ref 25).

In comparison with cross sections of $T_{300}$ (Fig. 7e and 8e) and $T_{500}$ (Fig. 7f and 8f), their interfaces have no delamination and intimate with partial–particle penetration of 0.5-3 μm into the substrate. These interface conditions suggest that bonding is more metallurgical as compared to mechanical interlocking because particles were not fully penetrated and enveloped in the substrate (Ref 34). The coating section was uniform with no inter-particle crack, suggesting the residual stress is more evenly distributed.

The porosity levels in the coatings increased with higher traverse speeds (Fig. 9a). The $T_{100}$ sample has a porosity level of 0.5%, while $T_{300}$ and $T_{500}$ have 2.7 and 3.2% porosity. The low porosity of $T_{100}$ sample was attributed to

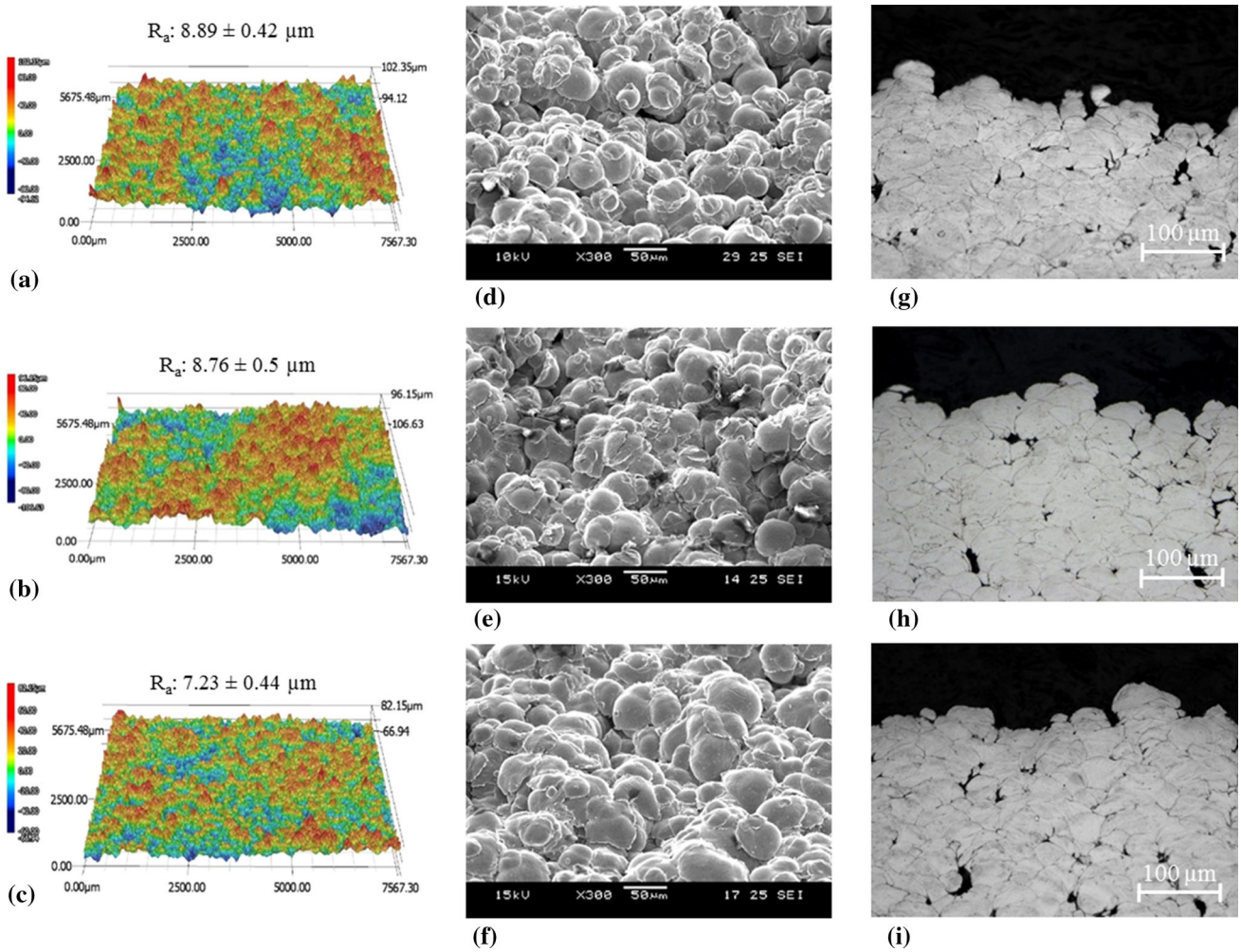


**Fig. 6** Surface topographies of (a) $T_{100}$, (b) $T_{300}$ and (c) $T_{500}$; SEM micrographs for surface morphologies of (d) $T_{100}$, (e) $T_{300}$ and (f) $T_{500}$; Optical micrographs of cross sections of top layer of (g) $T_{100}$, (h) $T_{300}$ and (i) $T_{500}$

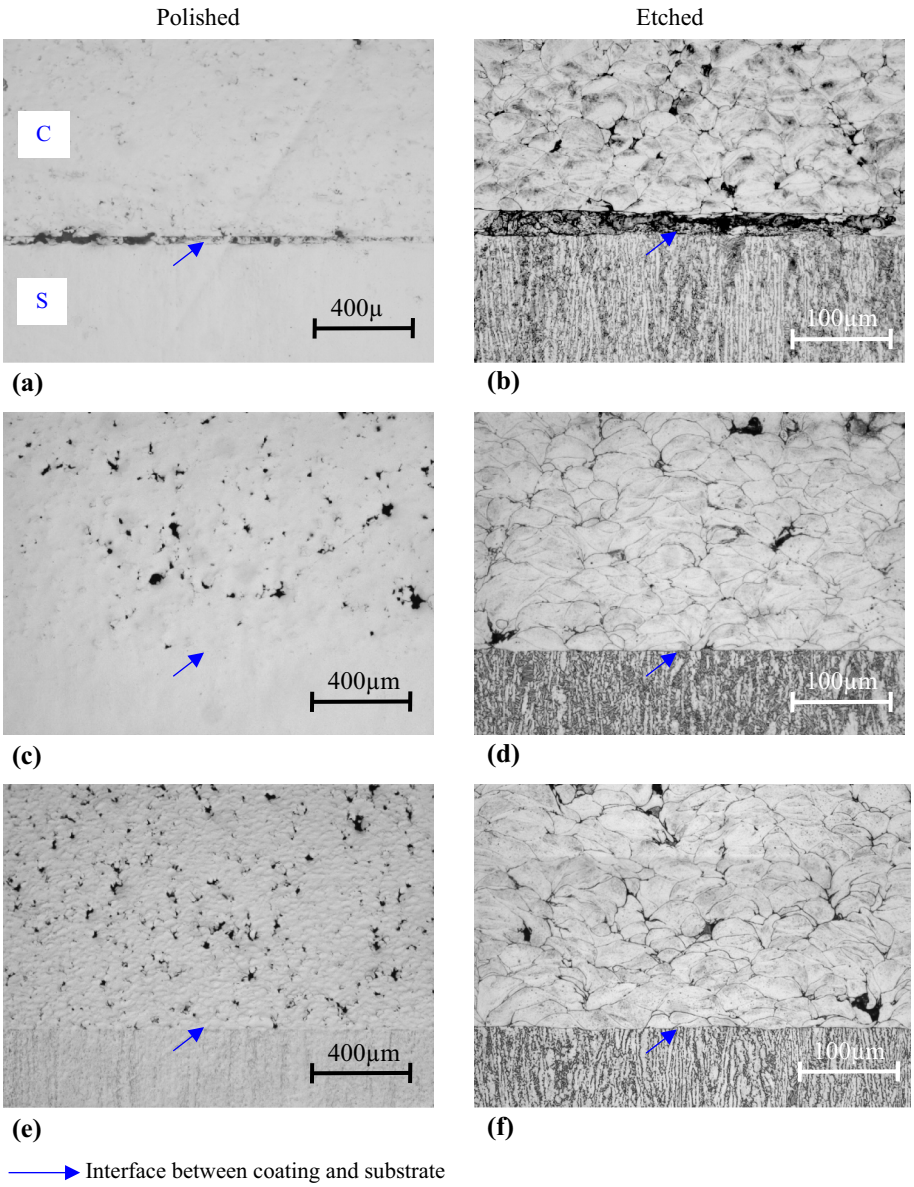


**Fig. 7** Optical micrographs of polished cross sections (a) $T_{100}$, (c) $T_{300}$ and (e) $T_{500}$; Optical micrographs of etched cross sections of (b) $T_{100}$, (d) $T_{300}$ and (f) $T_{500}$. The C and S in (a) denote the coating and substrate sections separated by the interface

the higher deposition temperature and highest coating thickness per layer (0.75 mm per layer). The large quantities of particles hammered the deposited thermally soften particles at high force and before the particles are allowed to cool off. This resulted in multi-direction plastic deformation of particles in the coating, which closes the inter-particle gap to form a dense coating, as shown in Fig. 10(a) and illustration in Fig. 10(d). Also, the higher thickness per layer will have higher thermal mass, which might act as a thermal reservoir and maintain the temperature of the next deposition layer.

The higher porosity levels of $T_{300}$ and $T_{500}$ sample was due to lower deposition temperature and coating thickness per layer, i.e., 0.28 and 0.13 mm, respectively. As a result, their particles were more uni-directional deformation (semi-spherical with jetting) and particles were work hardened and cooled before next deposition layer. This makes particles less malleable due to less thermal softening (Fig. 10b-c and illustration in Fig. 10d).

Figure 11 shows the average hardness of the coating deposited at different traverse speed. The hardness of the coating slightly decreased with increasing traverse speed. The overall hardness of all the coatings was still higher than the substrate ($323.5 \pm 3.26$ HV) and powder ($347.1 \pm 0.55$ HV, measured with nanoindentation). For the $T_{100}$ sample, the average hardness was $385.4 \pm 13.1$ HV, while for $T_{300}$ and $T_{500}$, the hardness was $377.3 \pm 7.7$ and $360.6 \pm 10.2$ HV respectively. This is because $T_{100}$ sample had more cold working than $T_{300}$ and $T_{500}$ as a result of multi-direction plastic deformation (Fig. 10d) and

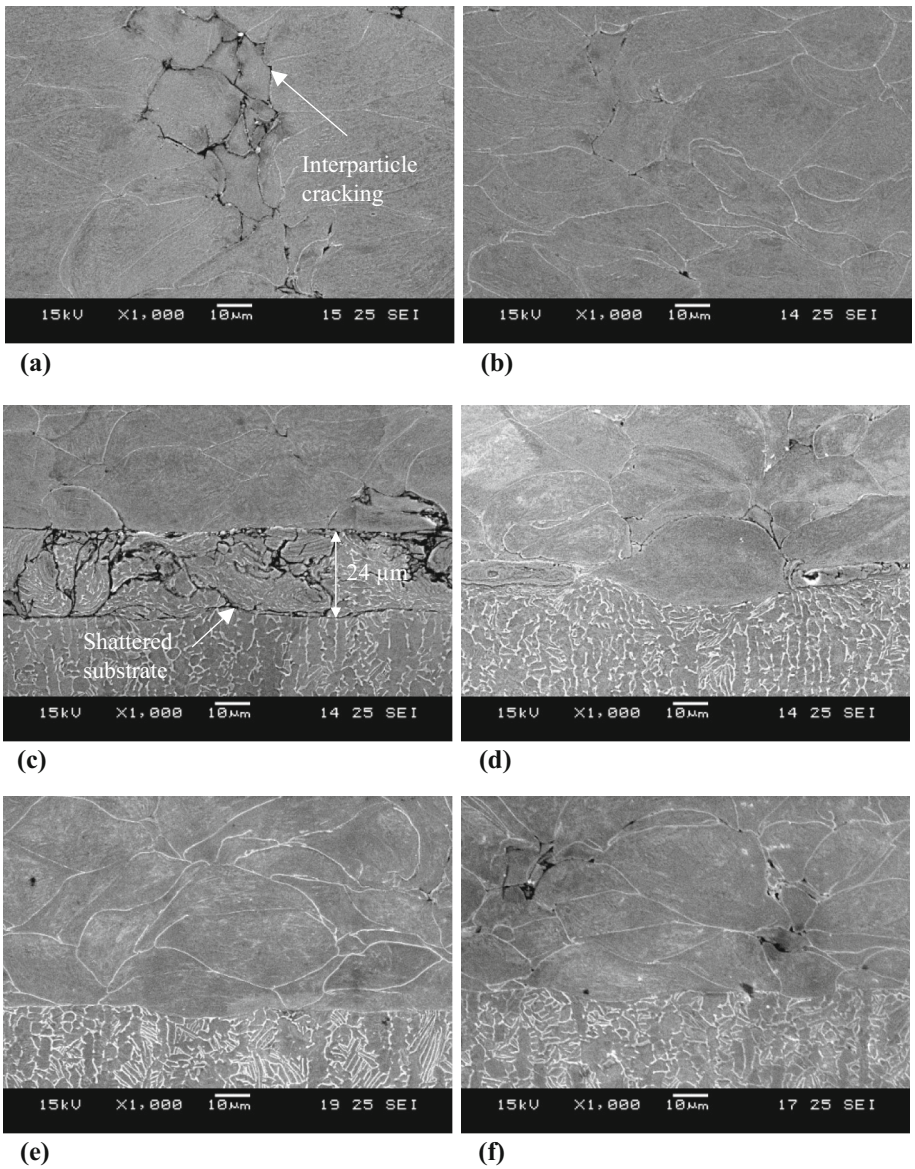


**Fig. 8** SEM micrographs of (a-d) $T_{100}$ cross section showing (a) inter-particle crack, (b) without inter-particle crack, (c) interface delamination, (d) without interface delamination; and interface condition of (e) $T_{300}$ and (f) $T_{500}$

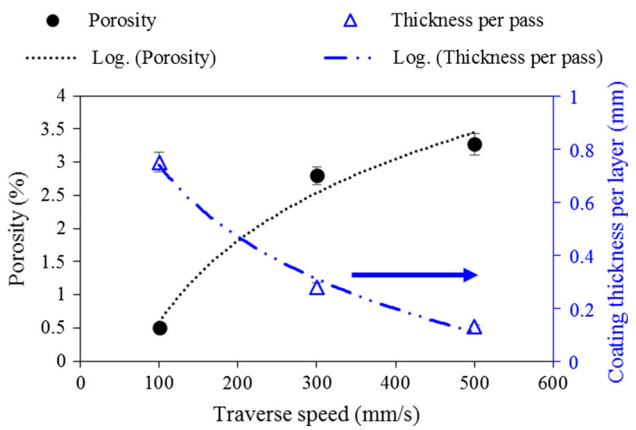


**Fig. 9** Porosity and coating thickness per pass as a function of traverse speed

denseness (low porosity) (Ref 16) and have induced more shear bands which consist of refined grains or nanograins (Ref 20). These decreased grains size reduces dislocation mobility and slipping which increase hardness can be described with the Hall–Petch equation:

$$H = H_{\infty} + kd_{\mathrm{g}}^{-\frac{1}{2}} \qquad \text{(Eq 3)}$$

where $H$ is the overall material hardness, $H_{\infty}$ is the initial material hardness $H_{\infty}$ (which is hardness of infinitely large grain size), $k$ is the constant, and $d_{\mathrm{g}}$ is the grain size.

The constant k in Eq 3 combines the effects of grain boundary strengthening and length of dislocations produced per unit area of grain boundary (Ref 20, 35). However, the $T_{100}$ sample had a larger standard deviation despite having larger average value, which showed that the

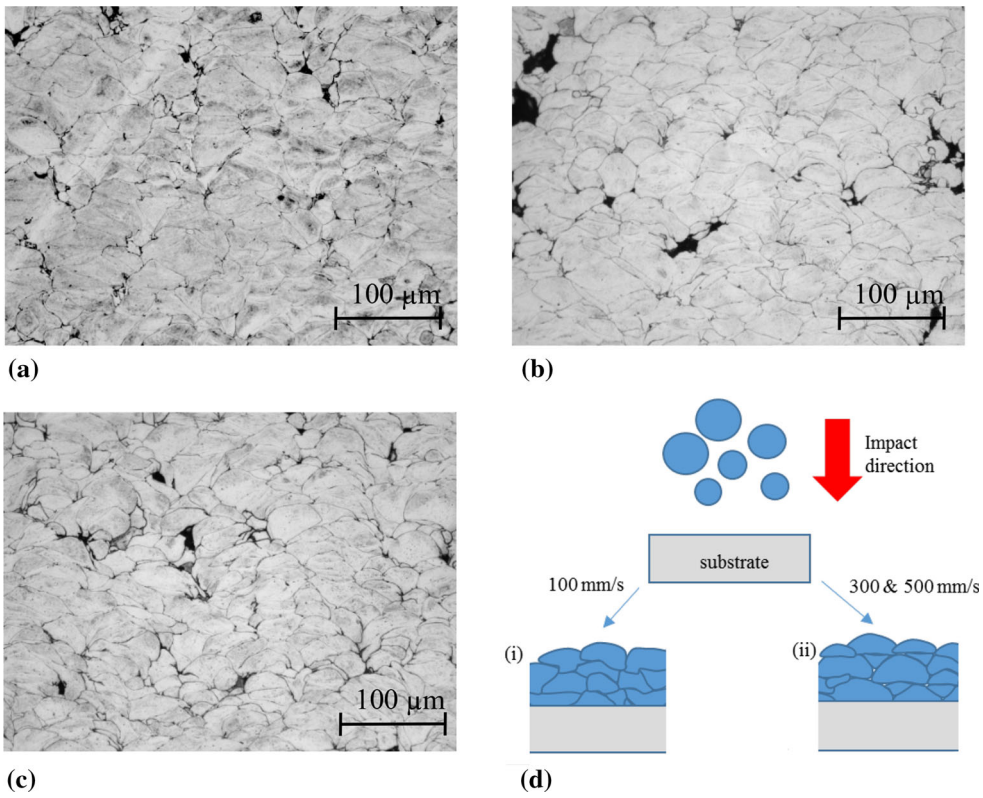


**Fig. 10** Optical micrographs of middle sections of etched coatings for (a) $T_{100}$, (b) $T_{300}$ and (c) $T_{500}$; and (d) illustration of unidirectional and multi-directional deformations from traverse speed variations

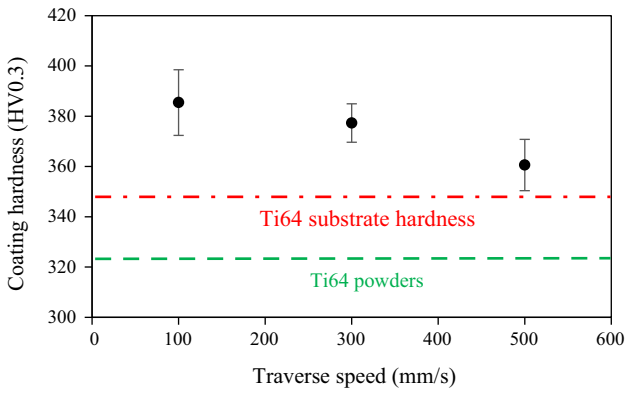


**Fig. 11** Hardness of coatings as a function of traverse speed. The red dotted lines represent the hardness of Ti64 substrate, while the green dotted line represents the hardness of Ti64 powder

cold working in the coating is not uniform. In comparison with a similar study on aluminum, the lower traverse for Ti64 deposition did not experience stress relief because the steady state temperature of around 315-366 °C is too low for any bulk (entire sample) phase change or recrystallization (Ref 26, 36).

## EDS and Phase Analysis

Both XRD and EDS (Fig. 12) results showed that the surfaces of Ti64 coatings deposited at multiple scan speeds have no impurities or phase transformation when compared to both the raw Ti64 powder and the uncoated Ti64 substrate. The phase transformation of Ti64 from $\alpha + \beta$ to $\beta$ requires at least 975 °C, whereas the measured temperature is not above 370 °C (Ref 37). In addition, the Ti64 powders were deposited at supersonic speeds where adiabatic shear bonding can occur within nanoseconds. Such a short exposure of the powder particles to the environment cannot induce significant atomic diffusion, such as the diffusion of nitrogen or oxygen (Ref 29). In addition, the impact of the particles can also disrupt surface oxide films on particles and substrates for bonding (Ref 38).

## Adhesion Strength

Figure 13 shows the adhesion strength test of the samples using setup illustrated in Fig. 13(b). Figure 13(a) shows that the $T_{100}$ sample de-bonded at its coating/substrate interface (Fig. 13c) at 2.5 MPa, while the $T_{300}$ and $T_{500}$ samples de-bonded at the glue bond line at 62.4 and 60.5 MPa, respectively (Fig. 13d). The failure at glue lines means that the coating adhesion strengths of $T_{300}$ and $T_{500}$ samples are above 60 MPa because the glue strength lies in the region of 60-75 MPa. The wide range of glue bond strength was due to stresses at the glue bond line which developed during curing (at 150 °C) of joined materials with different coefficient of thermal expansion (Ref 39). In

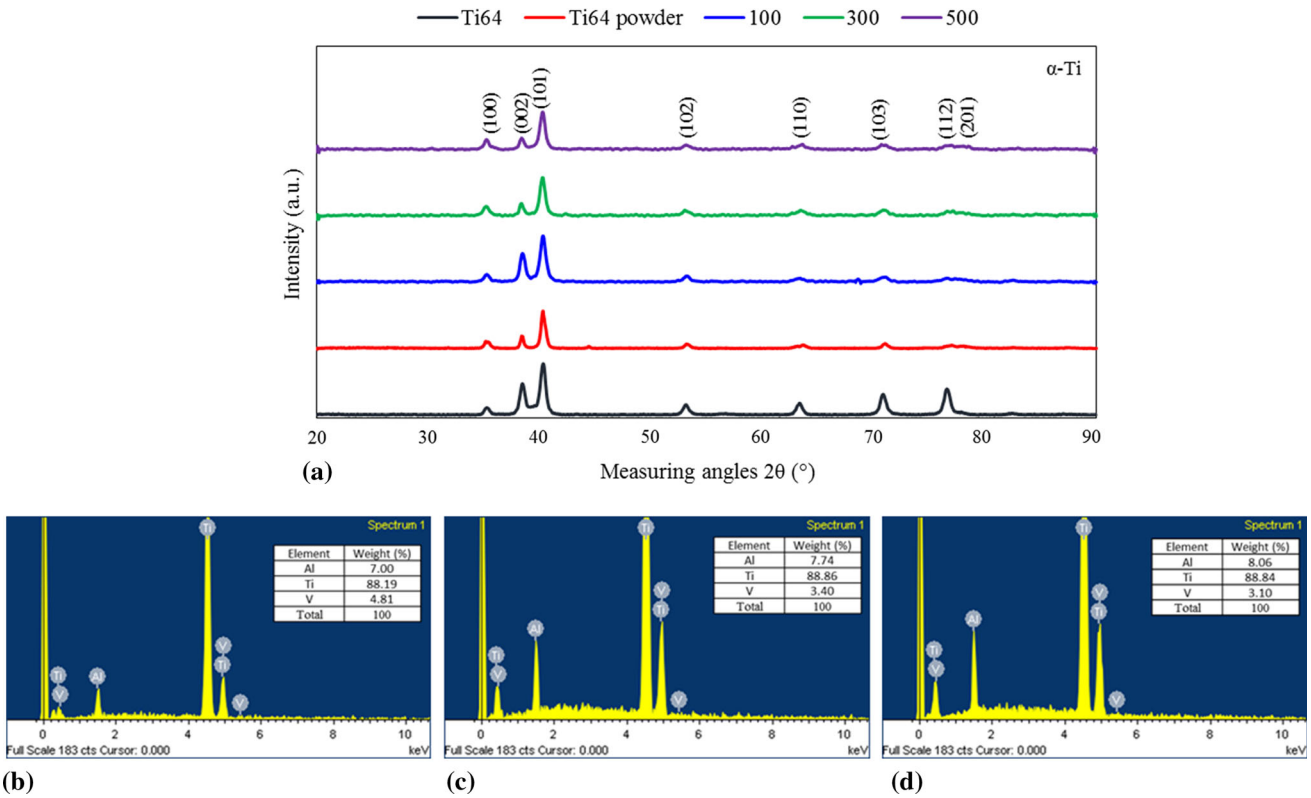


**Fig. 12** (a) XRD spectra of substrate, powder and samples; (b-d) EDS spectra for (b) $T_{100}$, (c) $T_{300}$ and (d) $T_{500}$

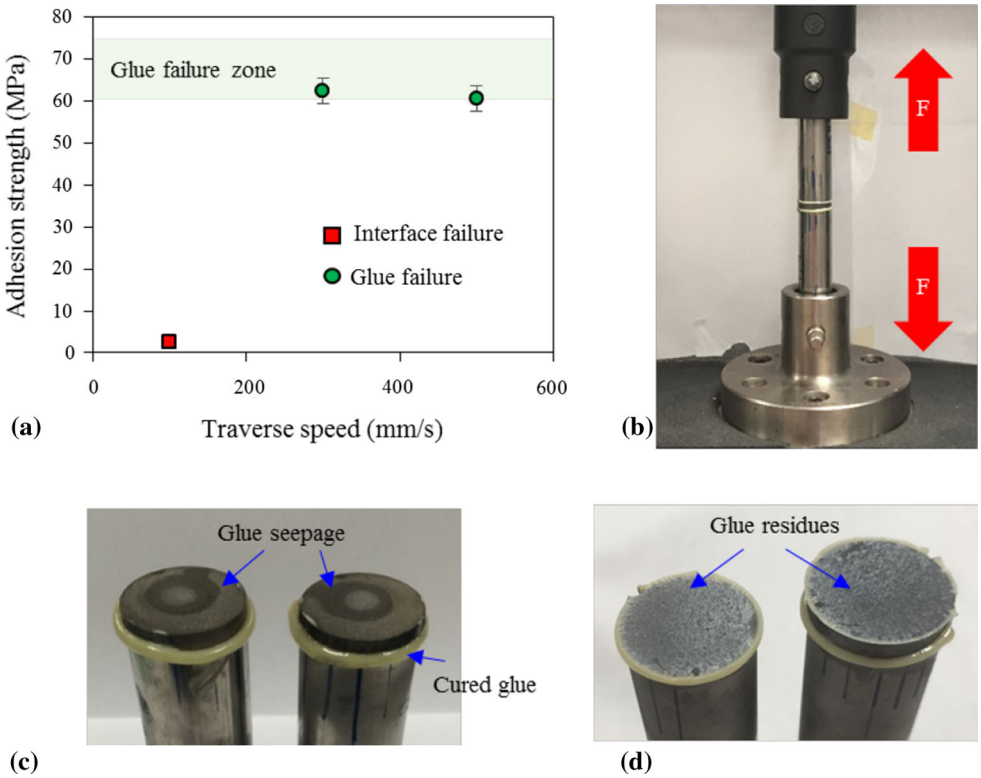


**Fig. 13** (a) Adhesion strength as a function of transverse speed, (b) adhesion test setup, (c) interface failure of $T_{100}$ sample and (d) glue failure of $T_{300}$ sample. The glue failure for $T_{500}$ is not shown due to its similarity with $T_{300}$ sample

this setup, the stainless fixture was glued with Ti64 with thermal expansion coefficients of 17.3 μm/m.°C and 8.64 μm/m.°C, respectively.

The $T_{100}$ sample was expected to have weak adhesion strength as it had delaminated before tensile testing (Fig. 8c). The coating delamination prior to glue curing also allowed some glue seepage from the exterior into the interface via capillary action (Fig. 13c) the during curing process, which has minimal impact on the result (unpressurized curing). As for the $T_{300}$ and $T_{500}$, the strong interface bonding is due to adiabatic shear bonding during particle impact, evident by the severe deformation with jetting of particles at the interface. Coating thickness can also affect adhesion strength, where thicker coating have higher residual stress which leads to poorer bond strength (Ref 40). For this case, the coating thickness played a minor effect because poor adhesion was caused shattered the sub-surface of substrate as a result of low traverse speed, i.e., (100 mm/s), which did not occur for faster traverse speed (300 and 500 mm/s).

## Fractography

Figure 14 shows the SEM analysis of the interface fracture of the coating and substrate for $T_{100}$ sample. The coating side showed protrusion of particles (Fig. 14a) which have rings of dimples (Fig. 14b). The dimples are indicative of ductile fracture in Ti64 and show metallurgical bonding occurred in that region (Ref 23, 37, 41, 42). At the center of the particles in Fig. 14(b), smooth dimple-free surfaces were observed which demonstrates no metallurgical bonding has taken place, as it does not undergo shearing action (Ref 19). The craters on the coating side were due to particles de-bonded and remained on the substrate during the tensile test (Fig. 14b).

On the substrate side in Fig. 14(c and d), some particles and craters can be seen on the surface. In Fig. 14(c), a group of particles remain adhered on substrate surface because some particles have weaker cohesive (inter-particle) bonding as compared to interface bonding (particles bonded at the interface). This consequently may have initiated a crack and allow de-bonding of this particle cluster. The craters were left by de-bonded particles which partially penetrated (0.5-2 μm) into the substrate (Fig. 14d). They were formed due to the impact of particles onto a thermally soften of the substrate surface.

Figure 15 shows the post-adhesion analysis of the cross section of $T_{300}$ and $T_{500}$ samples as the failure occurred at the glue instead of the interfaces. In the coating, the interface shows no signs of delamination and extensive inter-particle cracking. This reassures the coating quality even at 60 MPa tensile load. Besides, as these coatings were dense, no glue was seen in the coatings or at the

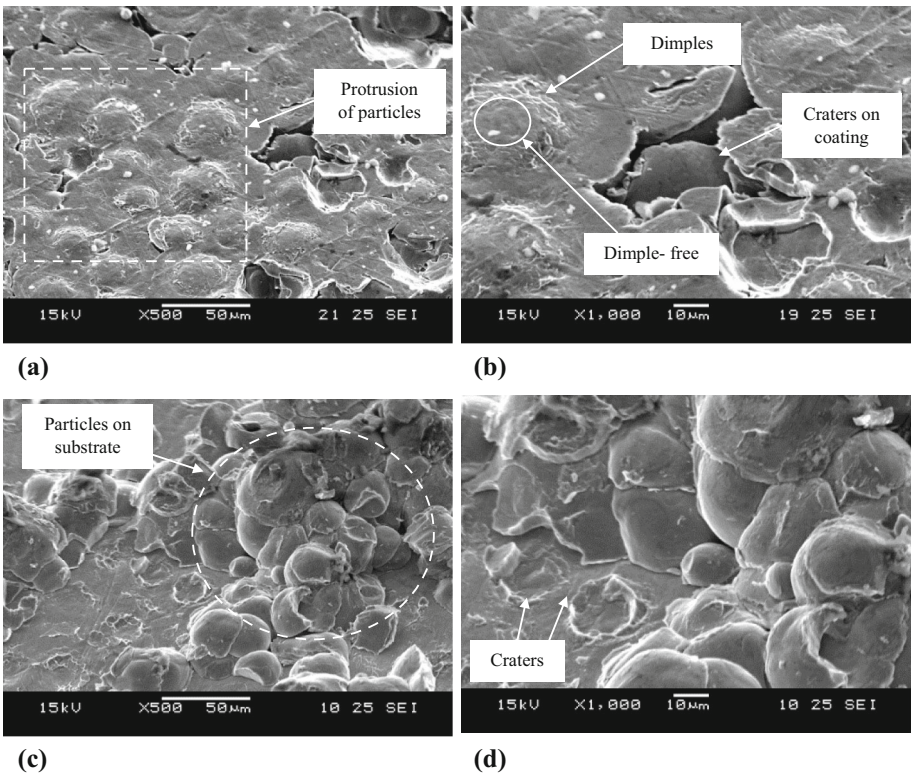


**Fig. 14** SEM micrographs showing fracture morphology of $T_{100}$ sample on (a and b) coating side and (c and d) substrate side at an angle of 45° with different magnifications

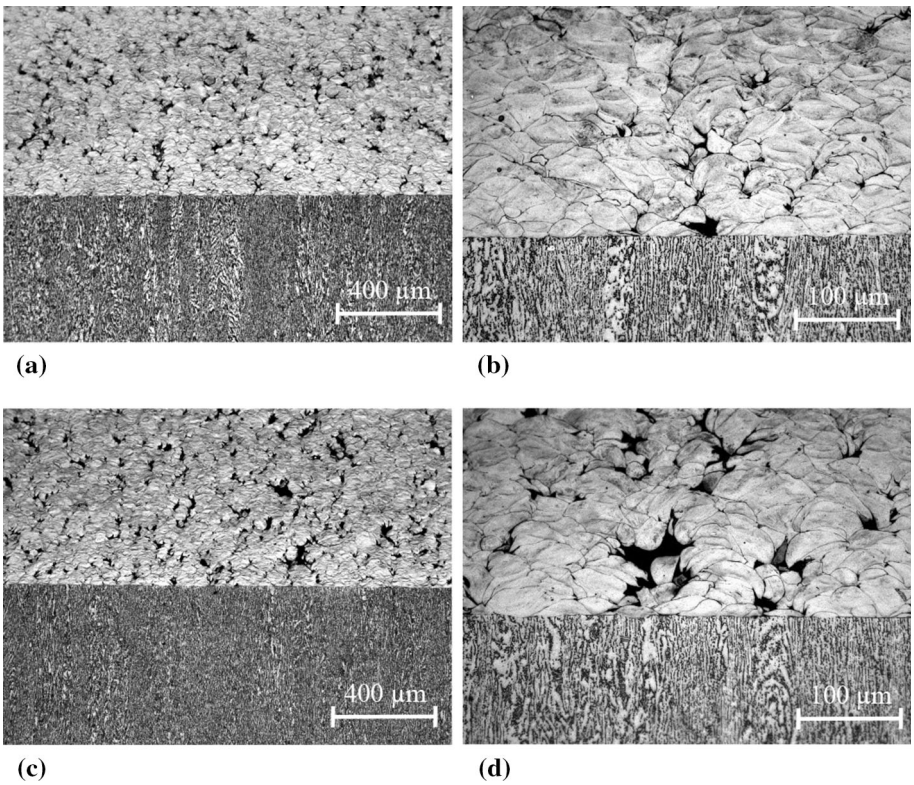


**Fig. 15** Optical micrographs showing post-adhesion views of cross sections of coatings deposited at 300 mm/s (a and b) and 500 mm/s (c and d), observed with different magnifications

interfaces through the post-adhesion cross-sectional views, which confirms no artificial strengthening.

## Conclusions

The effects of traverse scan speed of cold spray nozzle on the microstructure and mechanical properties of cold-sprayed Ti64 coatings were systematically studied. The temperature analysis showed that gas impingement and powder deposition at 100 mm/s traverse scanning speed had the largest heat accumulation followed by 300 and 500 mm/s. Heat tint was also observed on the substrate surface after gas impingement temperature measurement, where traverse speed of 100 mm/s resulted in purple color heat tint, while 300 and 500 mm/s showed a yellow color heat tint. The tint indicated a progressive nanoscale thickening of the surface oxide layer.

The coating surface morphologies among the samples showed no significant changes in deformation. As for the cross section, the coating deposited at 100 mm/s ($T_{100}$) had the lowest porosity level of about 0.5% while the coatings deposited at 300 ($T_{300}$) and 500 mm/s ($T_{500}$) had 2.7 and 3% porosity levels, respectively. However, the $T_{100}$ sample had interface delamination due to shattered sub-surface before any testing while $T_{300}$ and $T_{500}$ had strong interfaces. The XRD spectrum measured at the top surface and the EDS spectrum measured at the cross sections of each coating did not reveal impurities. The coating hardness decreased with increasing traverse speeds because of the deposition at lower traverse speeds allowed higher heat content, which resulted in multi-direction particle deformation, and translated to more strain hardening.

The adhesion tests showed that the sample corresponding to $T_{100}$ was the weakest, having an interface failure at 2.5 MPa, while those corresponding to $T_{300}$ and $T_{500}$ exceeded the glue strength of 60 MPa. The higher bond strengths of the samples corresponding to $T_{300}$ and $T_{500}$ were contributed by strong metallurgical bonding (due to lack of mechanical interlocking). The fractography of the sample corresponding to $T_{100}$ revealed that the substrate side had craters and adhered particles, while the coating side had protrusions of particles. Dimple fracture patterns were observed on the protruded particles as the signs of metallurgical bonding. For the samples corresponding to $T_{300}$ and $T_{500}$, the cross sections showed no significant signs of inter-particle or interface defects after the adhesion tests.

In summary, the traverse scanning speed significantly affected the microstructure and mechanical properties of the coatings and it has to be properly controlled.

**Acknowledgments** This work was financially supported by the National Research Foundation (NRF), Rolls-Royce (RR) and Nanyang Technological University (NTU), Singapore with the research grant (M-RT3.1: Metal Cold Spray). Authors appreciated the technical advice and support from Nicholas Weeks and Anna Tai.

## References

1. R.R. Boyer, Titanium for Aerospace: Rationale and Applications, *Adv. Perform. Mater.*, 1995, **2**(4), p 349-368
2. R.R. Boyer, An Overview on the Use of Titanium in the Aerospace Industry, *Mater. Sci. Eng. A*, 1996, **213**(1), p 103-114
3. J. Cizek, O. Kovarik, J. Siegl, K.A. Khor, and I. Dlouhy, Influence of Plasma and Cold Spray Deposited Ti Layers on High-Cycle Fatigue Properties of Ti6Al4V Substrates, *Surf. Coat. Technol.*, 2013, **217**, p 23-33
4. V.K. Champagne, *The Cold Spray Materials Deposition Process: Fundamentals and Applications*, 2007
5. R.C. Dykhuizen and M.F. Smith, Gas Dynamic Principles of Cold Spray, *J. Therm. Spray Technol.*, 1998, **7**(2), p 205-212
6. E. Irissou, J.G. Legoux, A.N. Ryabinin, B. Jodoin, and C. Moreau, Review on Cold Spray Process and Technology: Part I—Intellectual property, *J. Therm. Spray Technol.*, 2008, **17**(4), p 495-516
7. R.G. Maev and V. Leshchynsky, *Introduction to Low Pressure Gas Dynamic Spray: Physics & Technology*, 2008
8. A. Papyrin, Cold Spray Technology, *Adv. Mater. Processes*, 2001, **159**(9), p 49-51
9. A. Papyrin, V. Kosarev, S. Klinkov, A. Alkhimov, and V.M. Fomin, *Cold Spray Technology*, Elsevier, 2007
10. T. Schmidt, H. Assadi, F. Gärtner, H. Richter, T. Stoltenhoff, H. Kreye, and T. Klassen, From Particle Acceleration to Impact and Bonding in Cold Spraying, *J. Therm. Spray Technol.*, 2009, **18**(5-6), p 794-808
11. Efforts to Reduce Corrosion on the Military Equipment and Infrastructure of the Department of Defense, Office of the Secretary of Defense, 2007. http://corrdefense.nace.org/CorrDefense_Summer_2007/PDF/2007_DoD_Corrosion_Report.pdf
12. P. Fauchais and G. Montavon, Thermal and Cold Spray: Recent Developments, *Key Engineering Materials*, Vol 384, 2008, p 1-59
13. P. Vo, E. Irissou, J.G. Legoux, and S. Yue, Mechanical and Microstructural Characterization of Cold-Sprayed Ti-6Al-4V After Heat Treatment, *J. Therm. Spray Technol.*, 2013, **22**(6), p 954-964
14. W. Sun, A.W.Y. Tan, N.W. Khun, I. Marinescu, and E. Liu, Effect of Substrate Surface Condition on Fatigue Behavior of Cold Sprayed Ti6Al4V Coatings, *Surf. Coat. Technol.*, 2017, **320**, p 452-457
15. N.W. Khun, A.W.Y. Tan, and E. Liu, Mechanical and Tribological Properties of Cold-Sprayed Ti Coatings on Ti-6Al-4V Substrates, *J. Therm. Spray Technol.*, 2016, **25**(4), p 715-724
16. N.W. Khun, A.W.Y. Tan, W. Sun, and E. Liu, Effect of Heat Treatment Temperature on Microstructure and Mechanical and Tribological Properties of Cold Sprayed Ti-6Al-4V Coatings, *Tribol. Trans.*, 2016. doi:10.1080/10402004.2016.1244584
17. N.W. Khun, A.W.Y. Tan, K.J.W. Bi, and E. Liu, Effects of Working gas on Wear and Corrosion Resistances of Cold Sprayed Ti-6Al-4V Coatings, *Surf. Coat. Technol.*, 2016, **302**, p 1-12
18. X.-T. Luo, Y.-K. Wei, Y. Wang, and C.-J. Li, Microstructure and Mechanical Property of Ti and Ti6Al4V Prepared by an In-situ Shot Peening Assisted Cold Spraying, *Mater. Des.*, 2015, **85**, p 527-533
19. D. Goldbaum, J.M. Shockley, R.R. Chromik, A. Rezaeian, S. Yue, J.G. Legoux, and E. Irissou, The Effect of Deposition Conditions on Adhesion Strength of Ti and Ti6Al4V Cold Spray Splats, *J. Therm. Spray Technol.*, 2011, **21**(2), p 288-303
20. D. Goldbaum, R.R. Chromik, N. Brodusch, and R. Gauvin, Microstructure and Mechanical Properties of Ti Cold-Spray Splats Determined by Electron Channeling Contrast Imaging and Nanoindentation Mapping, *Microsc. Microanal.*, 2015, **21**(3), p 570-581
21. M. Perton, S. Costil, W. Wong, D. Poirier, E. Irissou, J.G. Legoux, A. Blouin, and S. Yue, Effect of Pulsed Laser Ablation and Continuous Laser Heating on the Adhesion and Cohesion of Cold Sprayed Ti-6Al-4V Coatings, *J. Therm. Spray Technol.*, 2012, **21**(6), p 1322-1333
22. M.V. Vidaller, A. List, F. Gaertner, T. Klassen, S. Dosta, and J.M. Guilemany, Single Impact Bonding of Cold Sprayed Ti-6Al-4 V Powders on Different Substrates, *J. Therm. Spray Technol.*, 2015, **24**(4), p 644-658
23. W.Y. Li, C. Zhang, X. Guo, J. Xu, C.J. Li, H. Liao, C. Coddet, and K.A. Khor, Ti and Ti-6Al-4V Coatings by Cold Spraying and Microstructure Modification by Heat Treatment, *Adv. Eng. Mater.*, 2007, **9**(5), p 418-423
24. A.M. Birt, V.K. Champagne, R.D. Sisson, and D. Apelian, Microstructural Analysis of Cold-Sprayed Ti-6Al-4V at the Micro- and Nano-Scale, *J. Therm. Spray Technol.*, 2015, **24**(7), p 1277-1288
25. S. Rech, A. Trentin, S. Vezzù, E. Vedelago, J.-G. Legoux, and E. Irissou, Different Cold Spray Deposition Strategies: Single- and Multi-layers to Repair Aluminium Alloy Components, *J. Therm. Spray Technol.*, 2014, **23**(8), p 1237-1250
26. W. Wong, E. Irissou, A.N. Ryabinin, J.-G. Legoux, and S. Yue, Influence of Helium and Nitrogen Gases on the Properties of Cold Gas Dynamic Sprayed Pure Titanium Coatings, *J. Therm. Spray Technol.*, 2010, **20**(1-2), p 213-226
27. http://www.arcam.com/wp-content/uploads/Arcam-Ti6Al4V-Titanium-Alloy.pdf
28. ASTM International, ASTM C633-13, Standard Test Method for Adhesion or Cohesion Strength of Thermal Spray Coatings, 2013
29. H. Assadi, F. Gärtner, T. Stoltenhoff, and H. Kreye, Bonding Mechanism in Cold Gas Spraying, *Acta Mater.*, 2003, **51**(15), p 4379-4394
30. G.B. Olson, J.F. Mescall, and M. Azrin, Adiabatic deformation and strain localization, *Shock Waves and High-Strain-Rate Phenomena in Metals: Concepts and Applications*, M.A. Meyers and L.E. Murr, Ed., Springer, New York, 1981, p 221-247
31. O. Untracht, *Jewelry Concepts & Technology*, Doubleday, New York, 2011
32. M.V. Diamanti, B. Del Curto, and M. Pedeferri, Interference Colors of Thin Oxide Layers on Titanium, *Color Res. Appl.*, 2008, **33**(3), p 221-228
33. N.K. Kuromoto, R.A. Simão, and G.A. Soares, Titanium Oxide Films Produced on Commercially Pure Titanium by Anodic Oxidation with Different Voltages, *Mater. Charact.*, 2007, **58**(2), p 114-121
34. T. Hussain, D.G. McCartney, P.H. Shipway, and D. Zhang, Bonding Mechanisms in Cold Spraying: The Contributions of Metallurgical and Mechanical Components, *J. Therm. Spray Technol.*, 2009, **18**(3), p 364-379
35. K.Y. Wang, T.D. Shen, M.X. Quan, and W.D. Wei, Hall-Petch Relationship in Nanocrystalline Titanium Produced by Ball-Milling, *J. Mater. Sci. Lett.*, 1993, **12**(23), p 1818-1820
36. M.K. McQuillan, Phase Transformations in Titanium and Its Alloys, *Metall. Rev.*, 1963, **8**(1), p 41-104
37. G. Lütjering and J.C. Williams, *Titanium*, Springer, New York, 2007

38. R.C. Dykhuizen, M.F. Smith, D.L. Gilmore, R.A. Neiser, X. Jiang, and S. Sampath, Impact of High Velocity Cold Spray Particles, *J. Therm. Spray Technol.*, 1999, **8**(4), p 559-564
39. https://www.generaladhesivos.com/new2/docs/TDS%20ARALDITE%20AV%20170.pdf
40. D.J. Greving, J.R. Shadley, E.F. Rybicki, D.J. Greving, J.R. Shadley, and E.F. Rybicki, Effects of Coating Thickness and Residual Stresses on the Bond Strength of ASTM C633-79 Thermal Spray Coating Test Specimens, *J. Therm. Spray Technol.*, 1994, **3**(4), p 371
41. W.-Y. Li, C. Zhang, X. Guo, C.-J. Li, H. Liao, and C. Coddet, Study on Impact Fusion at Particle Interfaces and its Effect on Coating Microstructure in Cold Spraying, *Appl. Surf. Sci.*, 2007, **254**(2), p 517-526
42. V.A. Joshi, *Titanium Alloys: An Atlas of Structures and Fracture Features*, Crc Press, Boca Raton, 2006